RESEARCH ARTICLE

NANO · MICRO small
www.small-journal.com

High Thermoelectric Performance Related to PVDF Ferroelectric Domains in P-Type Flexible PVDF-$Bi_{0.5}Sb_{1.5}Te_3$ Composite Film

Qinghui Jiang, Deng Pan, Yunfan Wang, Yong Liu, Yubo Luo, Junyou Yang, Baowen Li, Steve Dunn,* and Haixue Yan**

There is increasing demand to power Internet of Things devices using ambient energy sources. Flexible, low-temperature, organic/inorganic thermoelectric devices are a breakthrough next-generation approach to meet this challenge. However, these systems suffer from poor performance and expensive processing preventing wide application of the technology. In this study, by combining a ferroelectric polymer (Polyvinylidene fluoride (PVDF, β phase)) with p-type $Bi_{0.5}Sb_{1.5}Te_3$ (BST) a thermoelectric composite film with maximum is produced power factor. Energy filter from ferroelectric-thermoelectric junction also leads to high Seebeck voltage ≈242 µV K^{-1}. For the first time, compelling evidence is provided that the dipole of a ferroelectric material is helping decouple electron transport related to carrier mobility and the Seebeck coefficient, to provide 5× or more improvement in thermoelectric power factor. The best composition, PVDF/BST film with BST 95 wt.% has a power factor of 712 µW•m^{-1} K^{-2}. A thermoelectric generator fabricated from a PVDF/BST film demonstrated $P_{max}{}^{T}$ 12.02 µW and $P_{density}$ 40.8 W m^{-2} under 50 K temperature difference. This development also provides a new insight into a physical technique, applicable to both flexible and non-flexible thermoelectrics, to obtain comprehensive thermoelectric performance.

1. Introduction

Future on-person diagnostics and Internet of Things (IoT) devices require low-power sources. Replacing the battery with a sustainable power source is an ambition to improve reliability. IoT systems operate in ambient environments. As such harvesting thermal energy from the human body has aroused considerable interest.[1] In particular, attention has been paid to low-cost, flexible, and efficient thermoelectric (TE) systems. These would supply the required energy for low-power micro-devices such as wireless sensors, wearable technology, and extreme weather clothing.[2]

Power factor, represented by the product of electrical conductivity (σ) and the square of the Seebeck coefficient (S), directly influences the ability of a thermoelectric material to efficiently convert temperature gradients into electric current. A high power factor is essential for achieving high thermoelectric efficiency (also associated with TE figure of merit (ZT)), as it enables the generation of larger electrical currents at the same temperature gradient. For advanced thermoelectrics, these key parameters are comprehensively reflected in a radar chart, as Figure S1 (Supporting Information), to compare the thermoelectric performance of thermoelectric (TE) systems for IoT.

Inorganic TE film like Ag_2Se or Bi_2Te_3 have a high power factor after optimizing composition[3] or processing.[4] However,

Q. Jiang, D. Pan, Y. Luo, J. Yang
State Key Laboratory of Materials Processing and Die and Mould Technology
and School of Materials Science and Engineering
Huazhong University of Science and Technology
Wuhan, Hubei 430074, P. R. China
E-mail: qhjiang@hust.edu.cn

Y. Wang, B. Li
State Key Laboratory of Advanced Technology for Materials Synthesis and Processing
Center of Smart Materials and Devices
Wuhan University of Technology
Wuhan P. R. China, 430070

Y. Liu
Foshan (Southern China) Institute for New Materials
Foshan Guangdong 528220, P. R. China

S. Dunn
School of Engineering
London South Bank University
103 Borough Road, London SE1 0AA, UK
E-mail: dunns4@lsbu.ac.uk

H. Yan
School of Engineering and Materials Science
Queen Mary University of London
Mile End Road, London E1 4NS, UK
E-mail: h.x.yan@qmul.ac.uk

The ORCID identification number(s) for the author(s) of this article can be found under https://doi.org/10.1002/smll.202306786

DOI: 10.1002/smll.202306786

their high processing temperature (high cost) and limited scalability and flexibility are the barriers for flexible devices. Organic thermoelectric polymers such as Poly (3,4-ethylenedioxythiophene)/poly (styrenesulfonate) attract attention as they are lightweight, have mechanical adaptability, nontoxic, and solution processable.[5] They, however, have lower Seebeck coefficient and efficiency compared with inorganic materials.

Organic/inorganic composites have high TE properties and are flexible.[6] One approach is to incorporate inorganic fillers in polymer matrices aiming for a high power factor. The performance of organic/inorganic composites depends on the conductive network formed by fillers influencing the power factor. Typically, the power factor of the composites can be improved by annealing[7] or hot pressing[8] processing methods. However, these post-processing methods are barriers to the cost-effective production of flexible thermoelectric devices. There is a huge challenge to make an impact by developing low-cost rapid processes for large-scale TE composite films.

Polyvinylidene fluoride (PVDF) is a thermoplastic resin with low thermal conductivity and excellent chemical stability. Previous systems PVDF include Bi_2Se_3/PVDF,[9] $Cu_{0.1}Bi_2Se_3$/PVDF,[10] Ta_4SiTe_4/PVDF/GDY,[11] and Ag_2Se/PVDF.[12] State-of-the-art $Cu_{0.1}Bi_2Se_3$/PVDF composites exhibit a power factor, of 103 μW m^{-1} K^{-2}, and Seebeck coefficient, −84 μV K^{-1} at 290 K. A 13% decrease in performance after 5000 bending cycles was found. In these composites, PVDF was only used as a binder improving adhesion and flexibility. Ta_4SiTe_4/PVDF/graphdiyne composite has a power factor of 489 μW•$m^{-1}K^{-2}$ and ZT≈0.2 at 300 K and its resistance is almost unchanged after 10 000 bending cycle with a diameter of 18 mm.[11] The TE performance is lower than those of thermoelectric-polymer-based, PEDOT: PSS, films,[13] and carbon nanotube-based flexible thermoelectric materials.[14]

A challenge remains to simultaneously increase electrical conductivity and Seebeck coefficient as these conflict for thermoelectric materials.[15] Band structure engineering or energy filtering mechanisms can enhance the electrical conductivity without significantly affecting the Seebeck coefficient,[16] and allow for an increased power factor. Therefore, there is a need to develop new mechanisms to decouple electrical conductivity and the Seebeck effect. The interplay between the electron transport in ferroelectric and metal[17] or semiconductor[18] junctions provides a new and unique possibility to enhance thermoelectric properties.

Herein, we introduce a PVDF polar β phase by Spark Plasma Annealing (SPA) into p-type $Bi_{0.5}Sb_{1.5}Te_3$(BST)//PVDF composite films. Ferroelectric polarization in PVDF decouples electric conductivity and Seebeck coefficient for PVDF/BST composites. This simultaneously enhances electric conductivity (7.6 times) and Seebeck coefficient (>20%). A PVDF/BST composite film with BST 95 wt.% shows electrical conductivity of 122.0 S•cm^{-1} and a power factor of 712 μW•$m^{-1}K^{-2}$. The power factor of 527 μW•$m^{-1}K^{-2}$ after 1000 bends ≈6 mm radius is 77% of the original value. This work highlights the possibility of enhancing carrier mobility and the Seebeck coefficient using ferroelectric polarization of the PVDF polar β phase. It also provides a new approach for the preparation of TE composite materials using a roll-to-roll compatible technique.

2. Results and Discussion

Figure 1 shows the fabrication process for PVDF/BST films. The composite slurry was prepared by ball-milling BST particles and PVDF solution (Figure 1a). The film was fabricated by tape casting on a flexible polyimide substrate (Figure 1b). Figure 1c shows photographs of the film (10×10 cm^2) produced in the laboratory. SPA (details in Figure 1d) with a SPA maximum power of 1 kW, a pulse width, of 20 ms, and an interval, of 2 ms, was used from the DC power supply at an annealing temperature of 300–340 °C for 10 min.

PVDF/BST films with different BST weight content (80 wt.%, 85 wt.%, 90 wt.%, 92.5 wt.%, and 95 wt.%) were fabricated by tape casting combined with SPA. Above BST 95 wt.%, there was not enough PVDF to act as a binder during tape casting. Figure S2 (Supporting Information) shows SEM and AFM images of PVDF/BST films at different BST contents. Samples show an average roughness, R_a, of ≈20 nm with BST particles randomly dispersed in the PVDF. The films, annealed by SPA between 300 and 340 °C look to be a quality in terms of microstructure compared to films prepared by cold pressed and annealed in air at 300 °C (Figure S3, Supporting Information).

Figure 2 shows the electrical properties of PVDF/BST films with BST from 80 to 95 wt.%. As BST content increases, the percolation threshold is approached, and BST particles start to touch (Figure S4, Supporting Information). For BST content 80 wt.% the samples are below the percolation threshold leading to a relatively low conductivity, 17.6 S cm^{-1}, and power factor of 77 μW•$m^{-1}K^{-2}$. Figure 2a, shows the carrier concentration, n_H, and the carrier mobility, μ_H, increasing with BST content due to the contribution of holes from BST. In Figure 2b, Seebeck coefficients increase with BST content according to the General Effective Medium theory.[19] An increase in interfaces between BST and PVDF allows ferroelectric polarization (Figure S2, Supporting Information) to further improve the Seebeck coefficient of PVDF/BST film. As a result, the film with BST 95 wt.% content has a Seebeck coefficient of 242 μV K^{-1}. This exceeds $Bi_{0.5}Sb_{1.5}Te_3$/PAN samples (160-175 μV K^{-1}).[20]

See **Table 1** for more comparisons on the power factor. BST 95 wt.% has a power factor of 712 μW•$m^{-1}K^{-2}$ (Figure 2c). This is 9 times higher than 77 μW•$m^{-1}K^{-2}$ measured for the BST 80 wt.% film. As shown in Table 1, the power factor of the film with BST 95 wt.% in our work is currently the champion value for BST or PVDF-based organic/inorganic flexible films. By applying SPA using a pulsed square wave it is possible to rapidly densify the composite in a process[21] that is highly scalable. The scalable manufacturing and acceptable power delivery make SPA-processed PVDF/BST composite films competitive in future commercial applications (Figure S5, Supporting Information).

Figure 3 shows AFM images of BST (95 wt.%)/PVDF films SPA processed at 340 °C for 10 min. Figure 3a shows topography with an average roughness of ≈20 nm and Figure 3b shows phase-response under an applied field (10 V). The flat surface indicates no chain reorientation from external stretching. The piezoelectric properties with 19 V (AC) at point 1 in Figure 3a was examined by piezoelectric force microscopy (PFM), as shown in Figure 3c. Piezoresponse phase-voltage hysteresis loops demonstrate switchable polarization of PVDF. Over 10 V there is an abrupt phase change for the film. Domain switching is shown by

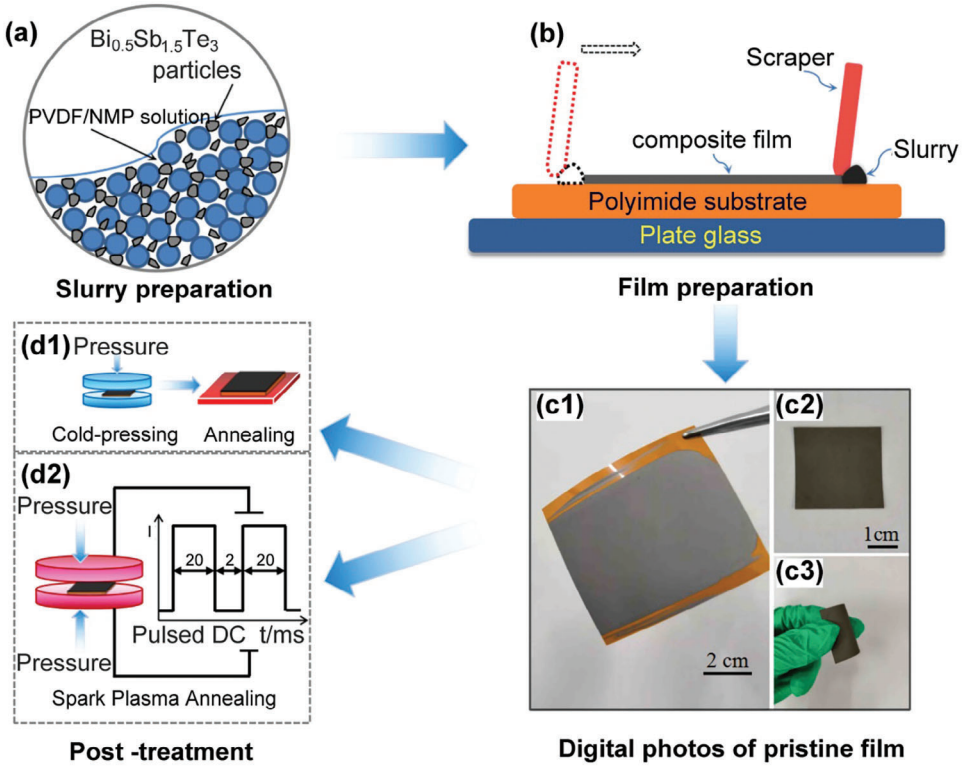

Figure 1. Schematic diagrams of preparation processes of PVDF/BST composite films. a), preparation of composite slurry. b), tape casting. c), digital photos. d), post-treatments of the pristine composite film.

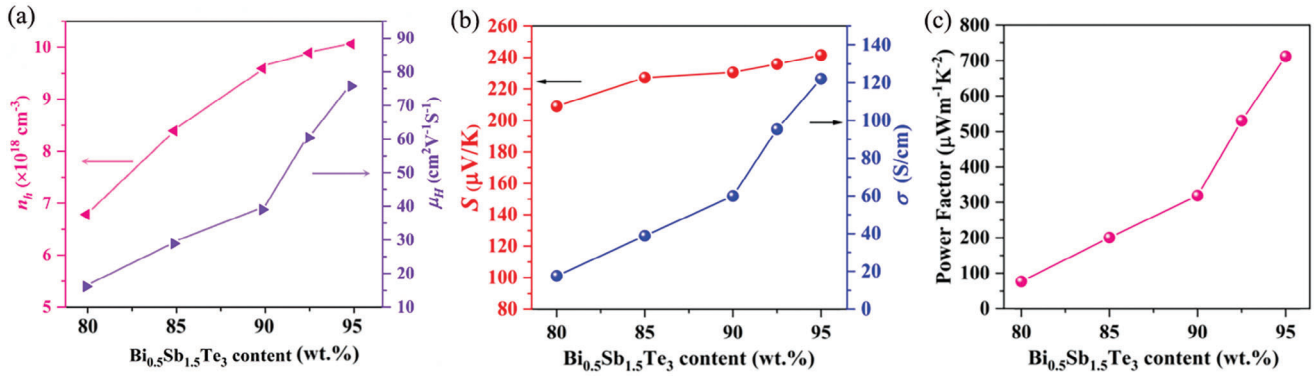

Figure 2. Electrical properties of PVDF/BST films with different BST weight contents by SPA at 340 °C for 10 min. a), electric transport properties. b), Seebeck coefficient and conductivity. c), power factor.

a change of phase signal when the voltage is reversed from −15 V to +15 V. The amplitude–voltage butterfly loops show changes of strain at DC voltages between 10 V and 15 V. Figure S6 (Supporting Information) can also show that applied tip bias of 10 V electric field can realize the abrupt inversion of the ferroelectric domains in this film. These features are indicative of ferroelectric switching. Figure 3d shows details of topography and phase along the line in Figure 3b. This indicates a range of nano-sized ferroelectric domains in PVDF with ≈52 peaks in 3.2 μm. These results show that SPA controls PVDF crystalline structures with PVDF polar β phase, which is consistent with the FTIR data (Figure S7, Supporting Information). It is noteworthy that the β phase transformation in the PVDF film was not induced by stretching.[33]

Electrical conductivity is higher in domain walls than in domains.[34] A higher domain wall density increases carrier conduction paths with associated increased carrier mobility for PVDF/BST films (see **Figure 4**a). In addition, a review of the microscopy (Figure S2, Supporting Information) shows the composite has a smooth and consistent interface. This results in reduced scattering and increased electron mobility (28.89 $cm^2 \bullet V^{-1}s^{-1}$) in films treated at 340 °C /10 min. A comparison of the impact of SPA treatment is shown in Figure 4b. The carrier concentration, 8.4×10^{18} cm^{-3}, for 340 °C /10 min treated

Table 1. Comparison of fabrication methods and power factor (PF, at room temperature) of different composite materials..

Materials	Methods	heat-treatment method	PF($\mu Wm^{-1}K^{-2}$)	Reference
PEDOT:PSS	Spin casting	5 vol.% of EG or DMSO	469	[22]
$Cu_{0.1}Bi_2Se_3$/PVDF	Drop casting	–	103.2	[9]
Ta_4SiTe_4/PVDF/GDY	Drop casting	Baking:120 °C, 10 hrs	489	[11]
Ni/PVDF	Drop casting	Annealing:110 °C, 30 mins	200	[23]
Ag_2Te/PVDF	Drop casting	–	30.9	[24]
BST/Te/Epoxy	Dispenser printing	Curing:250 °C,12 hrs	60	[25]
Bi_2Te_3/Se/Epoxy	Dispenser printing	Annealing:350 °C,12 hrs	270	[26]
BST/PLG	3D Extrusion	–	36	[27]
BST ink	Inkjet printing	Annealing:400 °C,30 mins	58	[28]
BST/Epoxy	Screen printing	Annealing:300 °C,6 hrs	123	[29]
BST/$C_{24}H_{44}O_6$	Brush printing	Annealing:400 °C,4 hrs	147	[30]
BST/PEDOT:PSS	Spin coating	Annealing:150 °C,10 mins	237	[31]
Carbon nanotube	ultrasonic spray	Annealing:130 ± 10 °C	340	[32]
PVDF/BST	Tape casting	SPA:340 °C,10 mins	711.9	This work

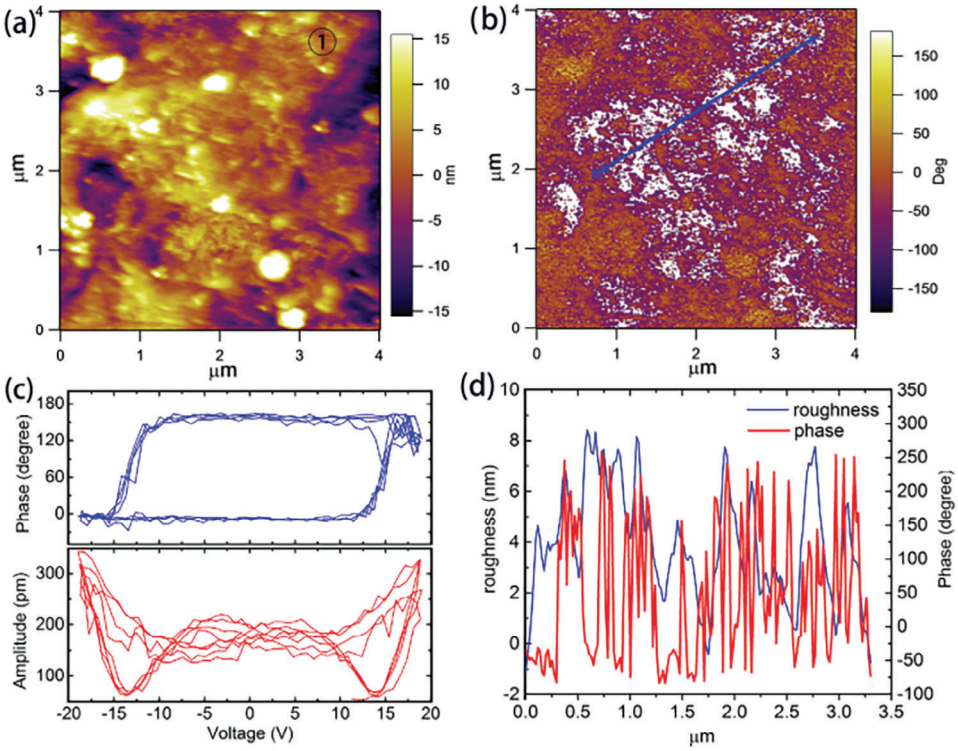

Figure 3. PFM morphologies of PVDF/BST films with 95 wt.% BST content by SPA at 340 °C for 10 min. a), topography image, and b), phase image under an applied field of 10 V. c), phase–voltage hysteresis loops and amplitude hysteresis loop up to 19 V at point 1 in Figure a). d), roughness and phase data along the blue line in Figure b).

films is not the highest for our samples. Therefore, we conclude there is an influence of interface quality and domain wall density related to the improvement in electrical conductivity.

As discussed in Figure 2a domain walls promote carrier mobility. Therefore, carrier mobility, μ_H, increases with PVDF/BST where domain walls are at the highest concentration. At BST 95 wt.%, carrier mobility was measured via the Hall effect as 75 $cm^2 \bullet V^{-1}S^{-1}$. This mobility approximates to single-phase BST and is higher than for BST-based composites such as 14–27 $cm^2V^{-1}S^{-1}$ in BST/SWCNT[35] and 45–50 $cm^2 \bullet V^{-1}S^{-1}$ in $Bi_{0.5}Sb_{1.5}Te_3$/Epoxy.[36] As we reach the percolation threshold for BST it becomes possible for particles to contact each other. This leads to an increase in electrical conductivity,[37] Figure 2b, such that the BST 95% film has a measured conductivity of

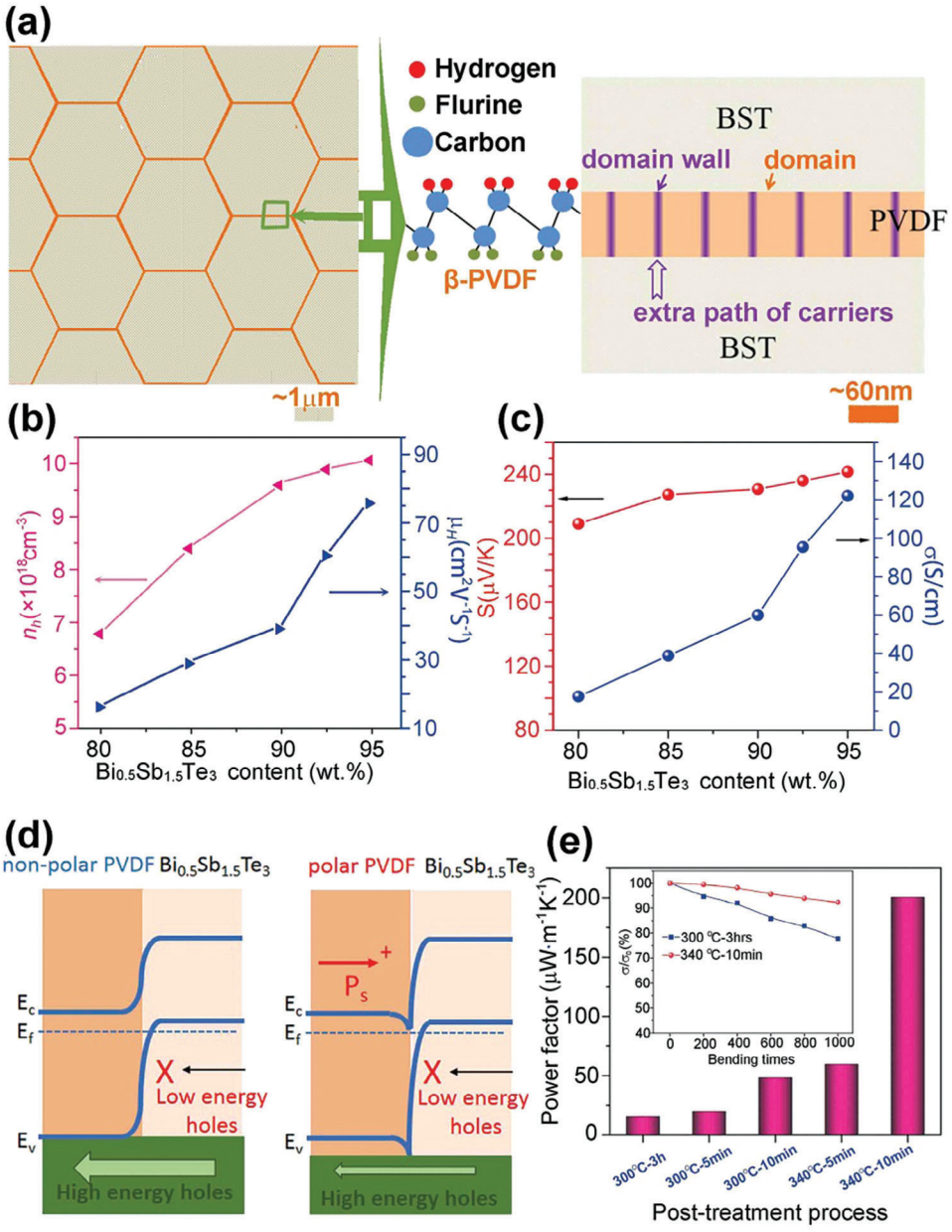

Figure 4. Schematic mechanism related to ferroelectric domains of PVDF in PVDF/BST films. a), the schematic diagram of the mechanism of high carrier mobility in PVDF/BST film. b), Hall carrier concentration, mobility, and electrical conductivity, and c), Seebeck coefficient of PVDF/BST composite films with 85 wt.% BST content under different post-treatments. d), the schematic representation of energy filtering effect in PVDF/BST film. e), power factor of PVDF/BST composite films with 85 wt.% BST content under different post-treatments. The inset of e is bending tests of PVDF/BST composite films under two post-treatments.

122.0 S cm^{-1}. This is 7 times as high as the film with BST 80 wt.%.

Figure 4b shows the electric properties of PVDF/BST films with 85 wt.% at room temperature after different post-casting treatments. Traditional annealing at 300 °C leads to an electrical conductivity of 3.68 S cm^{-1}. After SPA there are fewer voids and the conductive particles are closer resulting in a conductivity of 5.13 S cm^{-1}. The electrical conductivity was further increased by increasing the holding time or annealing temperature. By processing at 300 °C/10 min conductivity improved to 11.29 S cm^{-1}, while 340 °C/10 min led to a conductivity of 38.85 S cm^{-1}. The electric conductivity of 340 °C/10 min processed films is 7.6 times higher than that of the film with 300 °C/ 5 min, even though both films have similar microstructures and densities (Figure S3, Supporting Information). In Table S1 (Supporting Information) we show that single-phase BST samples fabricated at 300 and 340 °C have electric conductivities of 394 and 526 S cm^{-1}. This leads to the conclusion that in 85 wt.% BST film the ≈7.6 times improvement of electric conductivity across annealing temperatures is derived from the influence of PVDF polar phases on transport

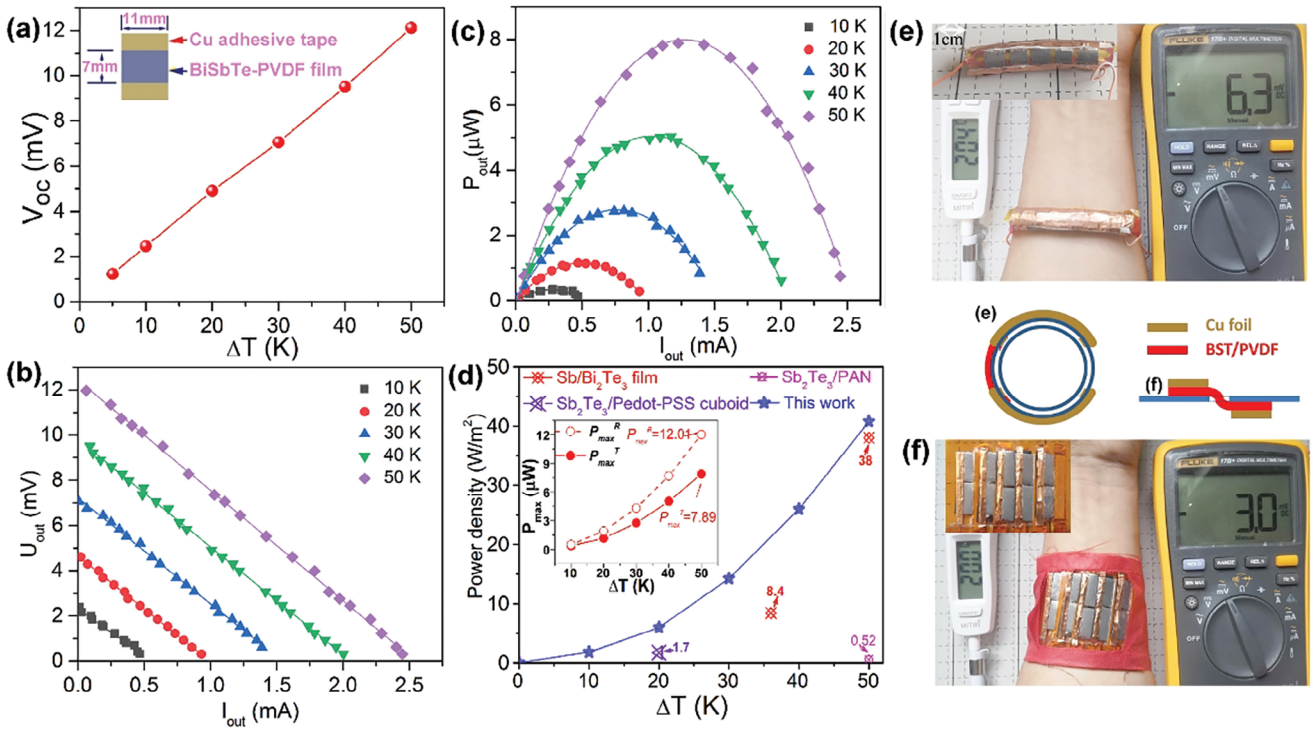

Figure 5. Device performance of single-leg TEG. a), V_{oc}-ΔT; b), U_{out}-I_{out}. c), P_{out}-I_{out}. d), P_{max}-ΔT curves. e,f), demonstration of flexible thermoelectric devices on the wrist.

behavior. Supporting evidence of the transition to polar PVDF can be found in Figures S6 and S7 (Supporting Information).

Seebeck coefficient is proportional to the difference of mean energy (E_J) and Fermi level (E_F), i.e., $S \propto (E_J - E_F)$.[38] It would be expected that the ferroelectric polarization of PVDF increases E_J for accumulated charge carriers. As shown in Figure 4c, the Seebeck coefficient (227 μV K^{-1}) of films processed at 340 °C for 10 min improved when compared to films sintered using traditional annealing, 200–205 μV K^{-1}, and BST sintered at 340 °C, 190 μV K^{-1} (Table S1, Supporting Information). PVDF has a wide bandgap[39] of ≈6.5 eV. The band gap, ≈0.2 eV, and electron affinity, 4.5 eV, of BST[40] leads to barriers for carrier migration at interfaces. Ferroelectric polarization will further distort band structure at interfaces. This distorted band structure blocks low and high energy carriers, see Figure 4d. This is energy filtering reducing carrier concentration in Figure 4b. Seebeck coefficient can be calculated using,[41]

$$S = \frac{8\pi^2 k_B^2}{3eh^2}\left(\frac{\pi}{3n}\right)^{2/3} m^* T \quad (1)$$

Where k_B, e, h, n, and m^* denote the Boltzmann constant, elementary charge, Planck constant, carrier concentration, and effective mass. There is a negative correlation with the Seebeck coefficient and carrier concentration. Based on our findings, ferroelectric polarization effectively decouples electrical conductivity and Seebeck coefficient in PVDF/BST films. This improves the power factor to 200.6 μW•$m^{-1}K^{-2}$ for SPA processed films ≈10x higher than 20 μW•$m^{-1}K^{-2}$ for PVDF/BST films prepared using traditional annealing at 300 °C in Figure 4e.

We show the impact of a bending radius of 6 mm on relative changes of performance in inset Figure 4e and Figure S8 (Supporting Information). PVDF leads to a composite PVDF/BST with good flexibility. The film with 85 wt.% BST produced by traditional annealing at 300 °C for 3 h exhibits a large number of voids. This reduces the stability of the structure (Figure S3, Supporting Information) enabling crack initiation during bending and a reduction in electrical conductivity. For traditionally annealed samples, electrical conductivity decreased by 22% over 1000 bending cycles. The film with 85 wt.% BST processed by SPA at 340 °C for 10 min electrical conductivity reduced by 7.7% over 1000 bending cycles. We attribute this to the high film density and quality of interfaces between BST and PVDF.

A single-leg thermoelectric generator with 7×11 mm was fabricated using 95 wt.% BST film. In **Figure 5** we show performance parameters. The internal resistance of the generator(the size is shown in the inset of Figure 5a) was 4 Ω. Figure 5a shows the open-circuit voltages (V_{oc}) under a range of ΔT. V_{oc} linearly increases with ΔT. The generator produces 12.1 mV at $\Delta T \approx 50$ K. Seebeck coefficient ≈242 μV K^{-1} can be calculated as the slope of Figure 5a, which is consistent with Figure 2b.According to Ohm's law,

$$U_{out} = E_{\Delta T} - I_{out} \cdot r_{in} \quad (2)$$

Where U_{out} is the output voltage, I_{out}, output current, r_{in}, internal resistance, $E_{\Delta T}$ is the Seebeck voltage of the TE generator and equal to the V_{oc} of the TE generator. As shown in Figure 5b, the output voltage U_{out} of TEG is linear with the output current I_{out}. Both parameters linearly increase with temperature difference,

whose product is output power P_{out} (Figure 5c). P_{out} increases with U_{out} and I_{out} reaching a maximum when load resistance equals internal resistance. Theoretical maximum output power, $P_{max}{}^{T}$, can be obtained from,

$$P_{max}^{T} = \frac{V_{oc}^2}{4r_{in}} = \frac{wt}{4l}\,\sigma \cdot S^2 \cdot \Delta T^2 \quad (3)$$

Where ΔT is the temperature difference between the hot and cold side of the leg, w is the width, l is the effective length, and t is the thickness of the composite film. According to Equation 3, at any temperature difference, $P_{max}{}^{T}$ is linear with power factor. A higher power factor leads to improved maximum output power. Meanwhile, $P_{max}{}^{T}$ and ΔT have a quadratic relationship, inset Figure 5d. For the TEG fabricated from BST95/PVDF, $P_{max}{}^{T}$ is 12.02 μW under $\Delta T \approx 50$ K. In reality, contact resistance leads to losses and reduced measured power.[42] This accounts for the difference in measured P^{T}_{max} of 7.89 μW at $\Delta T \approx 50$ K.

The power density was determined as follows:

$$P_{density} = \frac{P^{R}_{max}}{A} \quad (4)$$

where A is the cross-sectional area calculated from the width and thickness of the film. Figure 5d shows $P_{density}$ of the TEG measured to be 1.8, 6.0, 14.2, 26.0, and 40.8 W m^{-2}, at 10, 20, 30, 40, and 50 K temperature differences. $P_{density}$ of the present work is ≈100 times higher than previously reported for inorganic/organic composite-based TEG. Relevant examples are ≈0.52 W m^{-2} at 50 K of Sb_2Te_3/PAN[43] and ≈1.7 W m^{-2} at 19 K of Sb_2Te_3/PEDPT: PSS.[44] Additionally, our recorded $P_{density}$ for PVDF/BST SPA processed at 340 °C for 10 min exceeds single-phase inorganic films such as 8.4 W m^{-2} at 36 K of Bi_2Te_3/Sb_2Te_3 film hot-pressed for 2 h at 325 °C[45] and 38 W/m^2 at 50 K[46] in Bi_2Te_3/Sb_2Te_3 film annealed at 530 °C.

Two flexible devices were fabricated by connecting PVDF/BST film legs and copper wire with silver paste on a polyethylene tube or sheet, inset Figure 5e,f. The device in Figure 5e has 5 legs in series on a polyethylene tube with 10 mm diameter. A human wrist was used as the hot side. The device in Figure 5f has 5 legs in series and every leg has two PVDF/BST films in parallel decreasing internal resistance (all the legs have an effective size of 5×10 mm). One side of the legs is on a polyethylene sheet and the other side contacts a human wrist. The devices on the polyethylene tube and sheet have temperature differences of 5.3 and 2.5 K and generate voltage of 6.3 and 3.0 mV and maximum output power of 0.57 and 0.25 μW.

3. Conclusion

We have developed a Spark Plasma Annealing process to improve the performance of tape-cast flexible PVDF/BST films. The PVDF matrix is in the ferroelectric β phase after SPA processing. The ferroelectric polarization of PVDF influences electric transport properties through decoupling electrical carrier and phonon transport. This leads to simultaneous improvement in electric conductivity (7.8 times) and Seebeck coefficient (10%) of the best-performing films. As a result, a PVDF/BST film (85 wt.% BST) has maximum power factor (200.6 μW•m^{-1}K^{-2}), ten times higher than (about 20 μW•m^{-1}K^{-2}) of PVDF/BST film. The electrical properties of the film decrease by 7.7% after 1000 bending cycles around 6 mm. The best composition, PVDF/BST film with BST 95 wt.% has a power factor of 712 μW•m^{-1}K^{-2}. A TEG fabricated from a PVDF/BST film demonstrated $P_{max}{}^{T}$ 12.02 μW and $P_{density}$ 40.8 W m^{-2} under 50 K temperature difference. The combination of tape casting and SPA is a scalable and rapid fabrication process. Coupled with the improved power performance this enables the incorporation of PVDF/BST composites with SPA processing into devices as a viable technology to make flexible thermoelectric devices for future application.

4. Experimental Section

Preparation of Composite Slurry: Commercial p-type $Bi_{0.5}Sb_{1.5}Te_3$ ingot (Sagreon, China) was used as raw thermoelectric inorganic component (Seebeck coefficient 205±2 μV K^{-1}, electric conductivity 1000±50 S cm^{-1} and thermal conductivity 1.3±0.06 W•m^{-1}K^{-1} at room temperature). After ground by hand, the powders were high-energy ball milled for 3 h under the protection of an argon atmosphere by a high energy ball milling machine (SPEX 8000 M, CertiPrep, USA).

Polyvinylidene fluoride (PVDF, average molecular weight 400000, Aladdin) is used as an organic vehicle and binder. N-methylpyrrolidone (NMP, anhydrous 99.5%, Sigmaaldrich) is used as the solvent and diluent. PVDF/NMP solution was prepared with heating and magnetic stirring at 50 °C.

Finally, $Bi_{0.5}Sb_{1.5}Te_3$ powders and PVDF/NMP solution were mixed with different mass ratios of $Bi_{0.5}Sb_{1.5}Te_3$ and PVDF, and the composite slurries were obtained by ball milling at 300 rpm for 2 h in 200 ml pots with the steel balls with the diameter of 5 mm (Planetary ball milling, Nanda Company).

Preparation of $Bi_{0.5}Sb_{1.5}Te_3$/PVDF Composite Film: The composite slurry was blade-coated on the polyimide substrate with a blade gap of 200 μm and dried in a vacuum at 50°C to remove organic solvents. The thickness of pristine composite films can be also tailored by the height of the blade (100, 200, 300, and 400 μm). The traditional method is the combination of cold pressing and heat treatment (annealing) at 300°C for 3 h in a vacuum. In this work, the spark plasma annealing process is simulated by Spark Plasma Sintering (SPS) equipment.

Characterization and Measurements: Phase analysis of $Bi_{0.5}Sb_{1.5}Te_3$/PVDF composite films was completed using an X-ray Diffraction (Shimadzu XRD-6100) with Cu-Kα radiation (0.1540 nm) with the scanning speed of 10°min^{-1} (Figures S9–S11, Supporting Information). Scanning Electron Microscopes (NanoSEM 450, FEI Netherlands and GeminiSEM300, Carl Zeiss Germany) were used to observe the microstructure of the films (the fracture surface of the film is shown in Figure S12, Supporting Information). An atomic force microscope (SPM 9700, Shimadzu, Japan) was used to observe the surface microstructure of the films. The samples were scanned in the area of 30 μm×30 μm with a lateral resolution ≈0.2 nm. The piezoelectric response was obtained using a cantilever with an Au conductive coated tip in a piezoresponse force microscope (PFM) (Cypher ES, Oxford).

Differential Thermal Analysis and Thermogravimetric Analysis of PVDF and composite film were performed using a Diamond TG/DTA (Perkin Elmer) device from room temperature to 500 °C under a nitrogen atmosphere with a heating rate of 10 °C min^{-1} (Figure S13, Supporting Information).

The Seebeck equipments (lab-made equipment and ZEM-3, ULVAC) were used to test the Seebeck coefficient of the composite films at room temperature based on a dynamic method related with ΔV and ΔT. The in-plane electrical conductivity, Hall mobility, and carrier concentration of the films at room temperature were measured by the Ecopia HMS-5500 Hall Effect Tester (magnetic field ≈0.55 T, and current 0–20 mA). The change in electrical conductivity before and after the test was used to characterize the merits of the flexibility(shown in Figure S14, Supporting Information).

A simple device was set up to measure the performance parameters of Figure 5a-d of one leg, shown in Figure S15 (Supporting Information).

Percolation Calculation and Thermal Conductivity Simulation of PVDF/BST Films: The transport behaviors such as electrical and thermal conductivity of composite were commonly empirically described by percolation theory. For example, in classical percolation theory, the electric/thermal conductivity of the composite in the conducting region can be described by the equation[31]:

$$\sigma = \sigma_f \left(\frac{\phi - \phi_c}{1 - \phi_c}\right)^t, \phi > \phi_c \quad (5)$$

where σ, σ_f, ϕ, ϕ_c, and t is the electric conductivity of the composite, the electric conductivity of the filter, he volume fraction of the conductive filter, the percolation threshold, and the critical exponent. When the volume fraction of the filter reaches the percolation threshold, there was a sharp increase in conductivity. As shown in Figure S4 (Supporting Information), the fits of electric conductivity data give ϕ_c 0.29 and t 2.1, which was similar to theory values (0.33 and 2.0) predicted based on the spheroidal[47]/isotropic[48] model.

The thermal conductivity of films is calculated using the General Effective Medium (GEM) theory whose equation is followed as[19]:

$$\varphi \frac{\kappa_f^{1/t} - \kappa^{1/t}}{\kappa_f^{1/t} + [(1-\varphi c)/\varphi c]\kappa^{1/t}} = (1-\varphi)\frac{\kappa^{1/t} - \kappa_m^{1/t}}{\kappa_m^{1/t} + [(1-\varphi c)/\varphi c]\kappa^{1/t}} \quad (6)$$

where κ_m, κ_f, and κ is the thermal conductivity of the matrix, the filter, and the composite film without consideration of the interfaces' effect. The thermal conductivity of BST[49] and PVDF[50] phase was 1.0 and 0.2 $W \bullet m^{-1}K^{-1}$, respectively. Then the thermal conductivity of PVDF/BST films with different BST contents can be calculated with $\phi_c = 0.29$ and $t = 2.1$ according to Equation (6), as shown in the inset of Figure S16 (Supporting Information). It increases with BST content and for 95 wt.% BST content, thermal conductivity is about 0.79 $Wm^{-1}K^{-1}$. (The estimated thermal conductivity should be higher than real thermal conductivity because the GEM model does not take into account the influence of the interface. *ZT* values can be calculated according to $ZT = TS^2\sigma/\kappa$, and the *ZT* values of composite films with 95 wt.% BST content is ≈0.27, as shown in Figure S16 (Supporting Information).

Experimental Thermal Conductivity of PVDF/BST Film: The composite slurry with 95 wt.% BST was also dried at 60 °C in a vacuum for 1 day, put into the graphite die with an inner diameter of 10 mm, and then consolidated to the bulk with a thickness ≈1 mm by the same SPA conditions and its thermal conductivity was measured using the laser flash diffusivity method with a NETZSCH LFA-427 equipment. The average value of thermal conductivity of composite with 95 wt.% was 0.547 (Figure S17, Supporting Information), which was 70 percent of the calculated value. This indicates that the interfaces of PVDF and BST could also effectively scatter phonon. κ can be calculated according to the equation $\kappa = \rho C_p D$ (ρ density, C_p specific heat capacity, and D thermal diffusivity). The ZT_{exp} value of composite film with 95 wt.% BST content is about 0.39.

Reference Properties of Inorganic BST Bulk: The BST powders after high energy balling for 3 hr were put into the graphite die with an inner diameter of 12.5 mm and then consolidated to the bulk with a thickness of 1–3 mm by spark plasma sintering at 300 °C and 340 °C for 10 min. Their electrical conductivity, Seebeck coefficient, and thermal conductivity are measured using ZEM-3 or NETZSCH LFA-427, shown in Table S1 (Supporting Information). The thermal conductivity of pure BST bulk pellet fabricated by SPS at 300–340 °C was about 0.63–0.68 $W \bullet m^{-1}K^{-1}$.

Supporting Information

Supporting Information is available from the Wiley Online Library or from the author.

Acknowledgements

This work was supported by the National Natural Science Foundation of China (52273293, 52172187, 51772019, and 51572098) and the Royal Society (IEC\NSFC\170290).

conflict of interest

The authors declare no conflict of interest.

Data Availability Statement

Research data are not shared.

Keywords

carrier mobility, ferroelectric, spark plasma, sustainable, tape casting

Received: August 8, 2023
Revised: November 20, 2023
Published online:

[1] Q. Zhang, Y. Sun, W. Xu, D. Zhu, *Adv. Mater.* **2014**, *26*, 6829.
[2] Y. Wang, L. Yang, X.-L. Shi, X. Shi, L. Chen, M. S. Dargusch, J. Zou, Z.-G. Chen, *Adv. Mater.* **2019**, *31*, 1807916.
[3] S. I> Kim, K. H. Lee, H. A. Mun, H. S. Kim, S. W. Hwang, J. W. Roh, D. J. Yang, W. H> Shin, X. S. Li, Y. H. Lee, G. J. Snyder, S. W. Kim, *Science* **2015**, *348*, 109.
[4] Z.-H. Zheng, X.-L. Shi, D.-W. Ao, W.-D> Liu, M. Li, L.-Z. Kou, Y.-X. Chen, F> Li, M. Wei, G.-X. Liang, P. Fan, G. Q. Lu, Z.-G. Chen, *Nat. Sustain.* **2023**, *6*, 180.
[5] S. Panigrahy, B. Kandasubramanian, *Eur. Polym. J.* **2020**, *132*, 109726.
[6] C. Wan, X. Gu, F. Dang, T. Itoh, Y. Wang, H. Sasaki, M. Kondo, K. Koga, K. Yabuki, G. J. Snyder, R. Yang, K. Koumoto, *Nat. Mater.* **2015**, *14*, 622.
[7] L. Wang, Z. Zhang, Y. Liu, B. Wang, L. Fang, J. Qiu, K. Zhang, S. Wang, *Nat. Commun.* **2018**, *9*, 3817.
[8] H. Chen, F. Ye, W. Tang, J. He, M. Yin, Y. Wang, F. Xie, E. Bi, X. Yang, M. Grätzel, L. Han, *Nature* **2017**, *550*, 92.
[9] C. Dun, C. A. Hewitt, H. Huang, J. Xu, C. Zhou, W. Huang, Y. Cui, W. Zhou, Q. Jiang, D. L. Carroll, *Nano Energy* **2015**, *18*, 306.
[10] S. V. N. Pammi, V. Jella, J.-S. Choi, S.-G. Yoon, *J. Mater. Chem. C* **2017**, *5*, 763.
[11] S. Qu, C. Ming, P. Qiu, K. Xu, Q. Xu, Q. Yao, P. Lu, H. Zeng, X. Shi, L. Chen, *Energy Environ. Sci.* **2021**, *14*, 6586.
[12] D. Park, H. Ju, J. Kim, *J. Ind. Eng. Chem.* **2021**, *93*, 333.
[13] O. Bubnova, Z. U. Khan, H. Wang, S. Braun, D. R. Evans, M. Fabretto, P. Hojati-Talemi, D. Dagnelund, J.-B. Arlin, Y. H. Geerts, S. Desbief, D. W. Breiby, J. W. Andreasen, R. Lazzaroni, W. M. Chen, I. Zozoulenko, M. Fahlman, P. J. Murphy, M. Berggren, X. Crispin, *Nat. Mater.* **2014**, *13*, 190.
[14] K. T. Park, Y. S. Cho, I. Jeong, D. Jang, H. Cho, Y. Choi, T. Lee, Y. Ko, J. Choi, S. Y. Hong, M.-W. Oh, S. Chung, C. R. Park, H. Kim, *Adv. Energy Mater.* **2022**, *12*, 2200256.
[15] W. Zhao, Z. Liu, Z. Sun, Q. Zhang, P. Wei, X. Mu, H. Zhou, C. Li, S. Ma, D. He, P. Ji, W. Zhu, X. Nie, X. Su, X. Tang, B. Shen, X. Dong, J. Yang, Y. Liu, J. Shi, *Nature* **2017**, *549*, 247.
[16] a) T. Zhu, Y. Liu, C. Fu, J. P. Heremans, J. G. Snyder, X. Zhao, *Adv. Mater.* **2017**, *29*, 1605884; b)Y. Pei, X. Shi, A. LaLonde, H. Wang, L. Chen, G. J. Snyder, *Nature* **2011**, *473*, 66.

[17] M. Y>. Zhuravlev, R. F. Sabirianov, S. S. Jaswal, E. Y. Tsymbal, *Phys. Rev. Lett.* **2005**, *94*, 246802.
[18] S. Li, Z. Zhao, J. Li, H. Liu, M. Liu, Y. Zhang, L. Su, A. I. Pérez-Jiménez, Y. Guo, F. Yang, Y. Liu, J. Zhao, J. Zhang, L.-D. Zhao, Y. Lin, *Small* **2022**, *18*, 2202507.
[19] G. Shekel, C. Barad, H. Hayun, Y. Sadia, Y. Gelbstein, *Phys. Chem. Chem. Phys.* **2018**, *20*, 16666.
[20] X. B. Zhao, S. H. Hu, M. J. Zhao, T. J. Zhu, *Mater. Lett.* **2002**, *52*, 147.
[21] Z. Shen, Z. Zhao, H. Peng, M. Nygren, *Nature* **2002**, *417*, 266.
[22] G.-H. Kim, L. Shao, K. Zhang, K. P. Pipe, *Nat. Mater.* **2013**, *12*, 719.
[23] Y. Chen, M. He, B. Liu, G. C. Bazan, J. Zhou, Z. Liang, *Adv. Mater.* **2017**, *29*, 1604752.
[24] C. Zhou, C. Dun, B. Ge, K> Wang, Z. Shi, G. Liu, D. L. Carroll, G. Qiao, *Nanoscale* **2018**, *10*, 14830.
[25] D. Madan, Z. Wang, A. Chen, R. Winslow, P. K. Wright, J. W. Evans, *Appl. Phys. Lett.* **2014**, *104*, 013902.
[26] D. Madan, Z. Wang, A. Chen, R.-c. Juang, J. Keist, P. K. Wright, J. W. Evans, *ACS Appl. Mater. Interfaces* **2012**, *4*, 6117.
[27] J. Peng, I. Witting, N. Geisendorfer, M. Wang, M. Chang, A. Jakus, C. Kenel, X. Yan, R. Shah, G. J. Snyder, M. Grayson, *Nat. Commun.* **2019**, *10*, 5590.
[28] Z. Lu, M. Layani, X. Zhao, L. P. Tan, T. Sun, S. Fan, Q. Yan, S. Magdassi, H. H. Hng, *Small* **2014**, *10*, 3551.
[29] Z. Yuan, X. Tang, Z. Xu, J. Li, W. Chen, K. Liu, Y. Liu, Z. Zhang, Z. Zhang, *Applied Energy* **2018**, *225*, 746.
[30] H. Wu, X. Liu, P. Wei, H.-Y. Zhou, X. Mu, D.-Q. He, W.-T. Zhu, X.-L. Nie, W.-Y. Zhao, Q.-J. Zhang, *J. Electron. Mater.* **2017**, *46*, 2950.
[31] K. Kato, H. Hagino, K. Miyazaki, *J. Electron. Mater.* **2013**, *42*, 1313.
[32] A. D. Avery, B. H. Zhou, J. Lee, E.-S. Lee, E. M. Miller, R. Ihly, D. Wesenberg, K. S. Mistry, S. L. Guillot, B. L. Zink, Y.-H. Kim, J. L. Blackburn, A. J. Ferguson, *Nat. Energy* **2016**, *1*, 16033.
[33] C. Ben Osman, S. Nowak, A. Garcia-Sanchez, Y. Charles, S. Ammar, S. Mercone, F. Mammeri, *Eur. Polym. J.* **2016**, *84*, 602.
[34] G. Catalan, J. F. Scott, *Adv. Mater.* **2009**, *21*, 2463.
[35] K. Ahmad, C. Wan, *Nanotechnology* **2017**, *28*, 415402.
[36] P. Li, X.-L. Nie, Y. Tian, W.-B. Fang, P. Wei, W.-T. Zhu, Z.-G. Sun, Q.-J. Zhang, W.-Y Zhao, *J. Inorg. Mater.* **2019**, *34*, 679.
[37] a) Q. Jiang, J. Yang, P. Hing, H. Ye, *Mater. Adv.* **2020**, *1*, 1038; b) C. W. Nan, Y. Shen, J. Ma, in *Annual Review of Materials Research*, (Eds.: D. R. Clarke, M. Ruhle, F. Zok), **2010**, Vol. *40*, pp. 131–151.
[38] C. a. Li, X. Guan, S. Yue, X. Wang, J. Li, H. Cheng, S. Wang, A. K. K. Kyaw, J. Ouyang, *J. Mater. Chem. A* **2021**, *9*, 16952.
[39] J. Choi, P. A. Dowben, S. Pebley, A. V. Bune, S. Ducharme, V. M. Fridkin, S. P. Palto, N. Petukhova, *Phys. Rev. Lett.* **1998**, *80*, 1328.
[40] H.-S. Kim, T. Kim, J. An, D. Kim, J. H. Jeon, S.-I. Kim, *Appl. Sci.* **2021**, *11*, 910.
[41] G. J. Snyder, E. S. Toberer, *Nat. Mater.* **2008**, *7*, 105.
[42] Y. Lu, Y. Qiu, K. Cai, Y. Ding, M. Wang, C. Jiang, Q. Yao, C. Huang, L. Chen, J. He, *Energy Environ. Sci.* **2020**, *13*, 1240.
[43] J. A. Lee, A. E. Aliev, J. S. Bykova, M. J. De Andrade, D. Kim, H. J. Sim, X. Lepró, A. A. Zakhidov, J.-B. Lee, G. M. Spinks, S. Roth, S. J. Kim, R. H. Baughman, *Adv. Mater.* **2016**, *28*, 5038.
[44] Y. Yang, H. Hu, Z. Chen, Z. Wang, L. Jiang, G. Lu, X. Li, R. Chen, J. Jin, H. Kang, H. Chen, S. Lin, S. Xiao, H. Zhao, R. Xiong, J. Shi, Q. Zhou, S. Xu, Y. Chen, *Nano Lett.* **2020**, *20*, 4445.
[45] Y. Lu, Y. Qiu, K. Cai, X. Li, M. Gao, C. Jiang, J. He, *Mater. Today Phy.* **2020**, *14*, 100223.
[46] S. J. Kim, J. H. We, B. J. Cho, *Ener. Environ. Sci.* **2014**, *7*, 1959.
[47] D. S. Mclachlan, M. Blaszkiewicz, R. E. Newnham, *J. Am. Ceram. Soc.* **1990**, *73*, 2187.
[48] W.-Z. Cai, S.-T. Tu, J.-M. Gong, *J. Compos. Mater.* **2006**, *40*, 2131.
[49] a) Q. Jiang, J. Yang, J. Xin, Z. Zhou, D. Zhang, H. Yan, *J. Alloys Compd.* **2017**, *694*, 864; b)C. Zhang, Z. Peng, Z. Li, L. Yu, K. A. Khor, Q. Xiong, *Nano Energy* **2015**, *15*, 688.
[50] J.-F. Brun, C. Binet, J.-F. Tahon, A. Addad, P. Tranchard, S. Barrau, *Synth. Met.* **2020**, *269*, 116525.